*Int. J. Heat Mass Transfer.* Vol. 27, No. 11, pp. 1953–1962, 1984
Printed in Great Britain

0017 9310/84 $3.00 + 0.00
Pergamon Press Ltd.

# Heat and momentum transfer around a pair of spheres in viscous flow

REUVEN TAL (THAU),† DAH NAIN LEE‡ and WILLIAM A. SIRIGNANO†

† Mechanical Engineering Department and ‡ Mathematics Department, Carnegie-Mellon University, Pittsburgh, PA 15213, U.S.A.

(*Received* 8 *July* 1982 *and in revised form* 11 *July* 1983)

**Abstract**—The Navier–Stokes and energy equations have been solved numerically for a pair of spheres in tandem at $Re = 40$ for two different spacings using bispherical coordinates. The solutions compare favorably with experimental results. The drag coefficient and the average Nusselt number of either sphere is always less than that of a single isolated sphere, the effect being much stronger on the downstream sphere.

## 1. INTRODUCTION

THERE has been recent interest in the problem of interaction between two burning droplets. Twardus and Brzustowski [1] solved Laplace's equation in bispherical coordinates for the diffusion field around two stationary droplets, as a function of the distance between the droplets, obtaining criteria for the flame shape as a function of droplet size, spacing and stoichiometry. Umemura *et al.* [2, 3] addressed the same problem, for droplets of equal or non-equal sizes and included Stefan flow as well as the energy equation in their model. Using the Schvab–Zeldovich transformation, Umemura *et al.* [2, 3] obtained the burning rate and the flame surface shape for pairs of burning droplets. Labowsky [4] used the method of images to solve the Laplace equations in the interdroplet field for two and more droplets and concluded that droplet lifetimes are longer as the spacing is reduced. Forced convection was excluded from the above-mentioned studies.

Rex *et al.* [5] studied experimentally the burning of pairs of fuel droplets. It was observed that as the spacing is reduced from larger values with negligible droplet interference, the burning rate increases, presumably because heat losses from the flame surface are reduced by the proximity of a second heat source. As the spacing is reduced, the burning rate reaches a maximum and then decreases as the spacing is further decreased. This decrease in the burning rate could be produced by the 'competition' for oxygen of the two droplets surrounded by one flame sheet. Sangiovanni and Kesten [6] studied experimentally the burning of linear arrays of droplets and found that the burning rate decreases monotonically as the spacing is reduced. The apparent discrepancy between the experimental works mentioned above could be caused by the presence of free convection in the experiments performed by Rex *et al.* [5] and of forced convection in the experiments performed by Sangiovanni and Kesten [6].

In real combustors, the Reynolds number based on fuel droplet diameter can be as high as 200. As indicated by Prakash and Sirignano [7, 8] and Lara-Urbaneja and Sirignano [9], the most important effect of forced convection on a droplet is creation of internal circulation within the droplet. The internal circulation changes the characteristic heating times of the droplets by an order of magnitude. Subsequently, the droplet vaporization characteristic significantly differs from that given by the $d^2$-law for stationary droplets. For that reason, the existing combustion analyses for pairs of droplets in the absence of convection are limited in their applications. As a first step in the study of the combustion of a pair of fuel droplets in the presence of forced convection, we address the problem of heat and momentum transfer around a pair of solid spheres in viscous flow, at intermediate Reynolds numbers. This problem has not been solved theoretically although a considerable amount of experimental work has been performed on the subject by Rowe and Henwood [10] and Tsuji *et al.* [11]. The only theoretical work on a pair of spheres in tandem is limited to $Re \ll 1$ [12]. In the above-mentioned works it was found that the drag coefficient of either sphere was always less than that of a single isolated sphere.

Rowe and Henwood [10] performed measurements of drag forces on two spheres in line as well as with the centerline inclined to the flow direction, as part of a broad study of a hydraulic model of a fluidized bed. The Reynolds number range considered was 32–96. Although this range is different from that considered by Tsuji *et al.* [11], the drag results of the two works are in reasonable agreement. In fact, Rowe and Henwood [10] indicate that the Reynolds number is not a critical parameter in a fluidized bed. The experimental apparatus used by Rowe and Henwood [10] was as follows: 1/2 in. (12.7 mm) spheres were made of polyethene. A small hole was drilled in the sphere and this was plugged with solder to make the overall density just greater than that of water. The sphere was supported by a 4 in. (101.6 mm) length of 0.007 in. (0.18 mm) Nichrome wire which was pushed into it. Most of the wire was supported by a water-filled glass tube. Distilled water was circulated through an open-topped Perspex tank. The water stream caused deflection which was measured by sighting a cathe-

## NOMENCLATURE

| | |
|---|---|
| $a$ | focal distance of bispherical system |
| $b$ | half-distance between sphere centers |
| $C_D$ | drag coefficient |
| $C_{DF}$ | friction drag coefficient |
| $C_{DP}$ | pressure drag coefficient |
| $C_P$ | specific heat |
| $d$ | diameter of sphere |
| $DA$ | increment in the $\eta$-direction |
| $DB$ | increment in the $\theta$-direction |
| $F$ | function defined in equation (25) |
| $h$ | heat transfer coefficient |
| $h_1, h_2, h_3$ | metric coefficients |
| $I$ | discretizing index in the $\eta$-direction |
| $J$ | discretizing index in the $\sigma$-direction |
| $l_R$ | length of recirculating zone |
| $Nu$ | Nusselt number, $hd/\lambda$ |
| $P$ | dimensionless pressure, $P/\frac{1}{2}\rho V_\infty^2$ |
| $Pe$ | Peclet number, $Re\,Pr$ |
| $Pr$ | Prandtl number, $\mu C_P/\lambda$ |
| $r_{max}$ | outer radius of computational domain |
| $Re$ | Reynolds number, $V_\infty d/\nu$ |
| $Re_a$ | Reynolds number defined using $a$, $V_\infty a/\nu$ |
| $S(I,J)$ | discretized stream-function |
| $T$ | temperature |
| $T(I,J)$ | discretized temperature |
| $T_s$ | surface temperature |
| $U(I,J)$ | scaled vorticity, defined in equation (28) |
| $V_\alpha$ | velocity component in the $\alpha$-direction |
| $V_\beta$ | velocity component in the $\beta$-direction |
| $WS$ | stream-function relaxation parameter |
| $WT$ | temperature relaxation parameter |
| $WU$ | vorticity relaxation parameter |
| $X$ | axial coordinate |
| $Y$ | coordinate perpendicular to the axis of symmetry. |

Greek symbols

| | |
|---|---|
| $\alpha$ | coordinate in orthogonal curvilinear system |
| $\beta$ | coordinate in orthogonal curvilinear system |
| $\eta$ | coordinate in bispherical system |
| $\theta$ | coordinate in bispherical system |
| $\theta_p$ | polar angle in spherical coordinate system |
| $\lambda$ | thermal conductivity |
| $\mu$ | viscosity |
| $\nu$ | kinematic viscosity |
| $\xi$ | vorticity |
| $\rho$ | density |
| $\phi$ | coordinate in orthogonal curvilinear system |
| $\psi$ | stream-function. |

Special symbols

| | |
|---|---|
| $(\,)^*$ | dimensionless variable |
| $(\,)_\infty$ | value of variable at infinity (unperturbed flow conditions) |
| $(\,)_s$ | separation. |

tometer on one edge. At small angles the deflection is proportional to the drag and an absolute value can be calculated from the measured submerged weight of the sphere and wire, the length of suspension and the observed deflection. With this apparatus, reduction in drag coefficients could be detected for a spacing of 30 diameters. The method used by Tsuji *et al.* [11] is similar in principle to that of Rowe and Henwood [10] but differs in the technical details. The Reynolds numbers considered were 125–880.

Mass transport (which is analogous to heat transfer) around two spheres at low Reynolds numbers (but high Peclet numbers!) has been studied by Aminzadeh *et al.* [13]. It was found that the overall Sherwood number for either sphere was always less than that of a single isolated sphere. The present work brings a numerical solution for the Navier–Stokes and heat transfer equation for a pair of spheres in tandem at intermediate Reynolds numbers.

## 2. SOLUTIONS OF THE NAVIER–STOKES AND ENERGY EQUATIONS IN BISPHERICAL COORDINATES

### 2.1. *Geometry*

The most convenient coordinate system for a pair of spheres in tandem is the orthogonal bispherical coordinate system (see Fig. 1). The various field properties are expressed in terms of the variables $(\eta, \theta)$, the third variable in the coordinate system $(\phi)$ vanishing due to axisymmetry. The cylindrical polar coordinates originating at the middle of the segment connecting the centers of the two spheres are given as

$$X = \frac{a \sinh \eta}{\cosh \eta - \cos \theta} \tag{1}$$

$$Y = \frac{a \sin \theta}{\cosh \eta - \cos \theta}. \tag{2}$$

The focal distance of the bispherical system is $2a$. The value of $\eta$ varies between $-\eta_0$ on the upstream sphere to $+\mathrm{n}_0$ on the downstream sphere and $\theta$ varies between zero on the symmetry axis upstream to the left (upstream) sphere and downstream to the right (downstream) sphere and $\pi$ on the axis of symmetry between the two spheres.

The centers of the spheres are located at

$$b = \pm \frac{a}{\tanh \eta_0}. \tag{3}$$

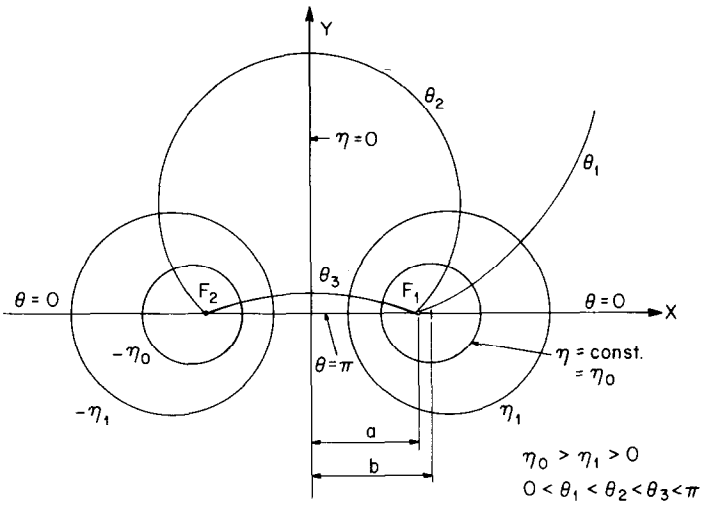


FIG. 1. Bispherical coordinate system.

The diameter of the spheres is

$$d = \frac{2a}{\sinh \eta_0}. \tag{4}$$

The ratio of the distance between the sphere centers and their diameter is

$$\frac{2b}{D} = \cosh \eta_0. \tag{5}$$

The metric coefficients for the bispherical coordinate systems are

$$h_1 = h_2 = \frac{a}{\cosh \eta - \cos \theta} \tag{6}$$

$$h_3 = \frac{a \sin \theta}{\cosh \eta - \cos \theta} \tag{7}$$

an element of length ds being calculated as

$$ds^2 = h_1^2 \, d\eta^2 + h_2^2 \, d\theta^2 + h_3^2 \, d\phi^2. \tag{8}$$

Some important features of the bispherical coordinate system should be mentioned here:

(1) The constant $\eta$ and constant $\theta$ lines are circles or arcs of circles.

(2) The value of $\theta$ for a given iso-$\theta$ line is equal to the angle between the tangent to this line and the axis of symmetry at the focus of the coordinate system.

(3) For a grid of uniform increments of $\Delta\theta$ and $\Delta\eta$, 50% of the grid points are located within a half circle centered at the origin with a radius equal to $a$ (half of the focal distance). The importance of this feature will be explained in context with the wake phenomena.

(4) This coordinate system is applicable even for two non-equal spheres in tandem. In such situations $\eta$ would vary from $-\eta_1$ to $+\eta_2$ ($|\eta_1| \neq |\eta_2|$), the bigger absolute value corresponding to the smaller sphere ($|\eta| \to \infty$ at the focal points). The diameters of the two spheres would be, in this case

$$d_1 = \frac{2a}{\sinh |\eta_1|} \tag{9}$$

$$d_2 = \frac{2a}{\sinh |\eta_2|}. \tag{10}$$

2.2. *Solution of the Navier–Stokes equation in bispherical coordinates*

The Navier–Stokes equations in the stream-function vorticity formulation for an axisymmetrical flow field in general orthogonal curvilinear coordinates $\alpha, \beta, \phi$ are written as

$$\xi = \frac{I}{h_1 h_2}\left[\frac{\partial}{\partial \alpha}\left(\frac{h_2}{h_3 h_1}\frac{\partial \psi}{\partial \alpha}\right) + \frac{\partial}{\partial \beta}\left(\frac{h_1}{h_2 h_3}\frac{\partial \psi}{\partial \beta}\right)\right] = \frac{1}{h_3} E^2 \psi \tag{11}$$

$$\frac{1}{h_1 h_2 h_3}\frac{\partial(\psi, E^2\psi)}{\partial(\alpha, \beta)} - \frac{2E^2\psi}{h_1 h_2 h_3^2}\frac{\partial(\psi, h_3)}{\partial(\alpha, \beta)} = \nu E^4 \psi. \tag{12}$$

The operator $E^2$ being defined as

$$E^2 = \frac{h_3}{h_1 h_2}\left[\frac{\partial}{\partial \alpha}\left(\frac{h_2}{h_3 h_1}\frac{\partial}{\partial \alpha}\right) + \frac{\partial}{\partial \beta}\left(\frac{h_1}{h_2 h_3}\frac{\partial}{\partial \beta}\right)\right]. \tag{13}$$

Using definition (13), equation (12) can be rewritten as

$$\frac{1}{h_1 h_2 h_3}\frac{\partial(\psi, h_3 \xi)}{\partial(\alpha, \beta)} - \frac{2\xi}{h_1 h_2 h_3}\frac{\partial(\psi, h_3)}{\partial(\alpha, \beta)} = \nu E^2 (h_3 \xi). \tag{14}$$

The velocity components in the $\alpha, \beta$ directions are calculated as

$$V_\alpha = -\frac{1}{h_2 h_3}\frac{\partial \psi}{\partial \beta} \tag{15}$$

$$V_\beta = \frac{1}{h_1 h_3}\frac{\partial \psi}{\partial \alpha}. \tag{16}$$

In order to express the Navier–Stokes equations in a dimensionless form, the following definitions are used

$$Re_a = \frac{V_\infty d}{\nu}\, a/d = Re\frac{\sinh \eta_0}{2}. \tag{17}$$

The dimensionless stream-function vorticity and velocity components are defined as

$$\psi^* = \frac{\psi}{V_\infty a^2} \tag{18}$$

$$\xi^* = \frac{\xi a}{V_\infty} \tag{19}$$

$$V_\alpha^* = \frac{V_\alpha}{V_\infty} \tag{20}$$

$$V_\beta^* = \frac{V_\beta}{V_\infty}. \tag{21}$$

In the case of a bispherical coordinate system after $\eta$ and $\theta$ are substituted for $\alpha$ and $\beta$ and $h_1$, $h_2$, $h_3$ are expressed explicitly, the Navier–Stokes equations become

$$U = (\cosh \eta - \cos \theta)^2\left[\frac{\partial F/\partial \eta}{F}\frac{\partial \psi^*}{\partial \eta} + \frac{\partial F/\partial \theta}{F}\frac{\partial^2 \psi^*}{\partial \eta^2} + \frac{\partial^2 \psi}{\partial \theta^2}\right] \tag{22}$$

$$Re_a F\left[\left(\frac{\partial \psi^*}{\partial \eta}\frac{\partial U}{\partial \theta} - \frac{\partial \psi^*}{\partial \theta}\frac{\partial U}{\partial \eta}\right) - 2U\left(-\frac{\partial \psi^*}{\partial \eta}\frac{\partial F/\partial \theta}{F} + \frac{\partial \psi}{\partial \theta}\frac{\partial F/\partial \eta}{F}\right)\right] = 1/F\frac{\partial F}{\partial \eta}\frac{\partial U}{\partial \eta} + 1/F\frac{\partial F}{\partial \theta}\frac{\partial U}{\partial \theta} + \frac{\partial^2 U}{\partial \eta^2} + \frac{\partial^2 U}{\partial \theta^2}. \tag{23}$$

The following definitions have been used

$$F = F(\eta, \theta) = \frac{\cosh \eta - \cos \theta}{\sin \theta} \tag{24}$$

$$U = \frac{\xi^*}{F}. \tag{25}$$

Equations (28) and (29) are written in a finite-difference form. The range between $-\eta_0$ to $+\eta_0$ is divided into 80 segments, the running index in the $\eta$-direction being $I$. The value of $\eta$ at any grid point is given as

$$\eta(I) = \frac{2\eta_0}{80}(I-1) - \eta_0 = DA(I-1) - \eta_0 \tag{26}$$

where $DA$ is the increment $2\eta_0/80$ in the $\eta$-direction.

Sixty divisions are taken in the $\theta$-direction discretized by the $J$ index. Thus

$$\theta(J) = \frac{\pi}{60}(J-1) = DB(J-1) \tag{27}$$

where $DB$ is the increment $\pi/60$ in the $\theta$-direction. Equations (28) and (29) in a finite-difference form become

$$\frac{U(I,J)}{SQ(I,J)} = \frac{F_\eta(I,J)}{F(I,J)}\frac{S(I+1,J)-S(I-1,J)}{2DA} + \frac{F_\theta(I,J)}{F(I,J)}\frac{S(I,J+1)-S(I,J-1)}{2DB} + \frac{S(I+1,J)+S(I-1,J)-2S(I,J)}{(DA)^2} + \frac{S(I,J+1)+S(I,J-1)-2S(I,J)}{(DB)^2} \tag{28}$$

$$Re_a \langle F(I,J)\rangle^2\left[\frac{S(I+1,J)-S(I-1,J)}{2DA}\cdot\frac{U(I,J+1)-U(I,J-1)}{2DB} - \frac{U(I+1,J)-U(I-1,J)}{2DA}\cdot\frac{S(I,J+1)-S(I,J-1)}{2DB}\right] + 2U(I,J)\,Re_a\left[F(I,J)F_\theta(I,J)\frac{S(I+1,J)-S(I-1,J)}{2DA} - F(I,J)F_\eta(I,J)\frac{S(I,J+1)-S(I,J-1)}{2DB}\right] = F_\eta(I,J)\frac{U(I+1,J)-U(I-1,J)}{2DA} + F_\theta(I,J)\frac{U(I,J+1)-U(I,J-1)}{2DB} + F(I,J)\frac{U(I+1,J)+U(I-1,J)-2U(I,J)}{(DA)^2} + F(I,J)\frac{U(I,J+1)+U(I,J-1)-2U(I,J)}{(DB)^2}. \tag{29}$$

The function $SQ(I,J)$ being calculated as

$$SQ(I,J) = [\cosh(\eta\langle I\rangle) - \cos(\theta\langle J\rangle)]^2. \tag{30}$$

The boundary conditions for the stream-function and the vorticity are:

(a) on the axis of symmetry ($\theta = 0$ and $\pi$), $\psi^* = 0$, $\xi^* = 0$ (thus $U = 0$),

(b) on the two spheres ($\eta = -\eta_0$ and $\eta_0$), $\psi^* = 0$,

$$U = \xi^*/F = (\cosh \eta - \cos \theta)|_{\eta = \pm\eta_0}(\partial^2 \psi^*/\partial \eta^2),$$

(c) on the outer edge of the computational domain ($r_{max}$) uniform parallel flow conditions prevail, thus

$$U = \xi^*/F = 0,$$

$$\psi^* = 1/2(r_{max}^2/a^2)\sin^2[\arctan\, y(\eta,\theta)/x(\eta,\theta)].$$

The outer edge of the computational domain is expressed in terms of $\eta$ and $\theta$ as $\theta = \theta_{min}(\eta)$, or in discretized form, $J = J_{min}(I)$. In our particular calculations, $r_{max}$ was given a value three times the distance between the forward stagnation point of the upstream sphere and the aft stagnation point of the downstream sphere.

Equations (34) and (35) are solved simultaneously by a successive overrelaxation (SOR) scheme.

The values of $\psi^*(I,J)$ and $U(I,J)$ are calculated as

$$\psi^*_{n+1}(I,J) = \psi^*_n(I,J) + WS[\psi^*_{n+1}(I,J) - \psi^*_n(I,J)] \quad (31)$$

$$U_{n+1}(I,J) = U_n(I,J) + WU\,[U_{n+1}(I,J) - U_n(I,J)], \quad (32)$$

where $WS$ and $WU$ are the relaxation factors for $\psi^*$ and $U$, respectively.

Overrelaxation is feasible for the stream-function equation but using the present scheme underrelaxation is mandatory for the vorticity equation. A factor of 1.2 was used for the stream-function while 0.2 was taken for the vorticity. This results in a somewhat high CPU time (typically 15 min on a DEC-20 system). A non-uniform spacing of the grid† would resolve this difficulty, but as it considerably complicates the finite-difference formulation it has not been presently pursued.

The velocity components are calculated from the stream-function solution as

$$V^*_\eta = \frac{-(\cosh\eta - \cos\theta)^2}{\sin\theta}\frac{\partial\psi^*}{\partial\theta} \quad (33)$$

$$V^*_\theta = \frac{(\cosh\eta - \cos\theta)^2}{\sin\theta}\frac{\partial\psi^*}{\partial\eta}. \quad (34)$$

## 3. SOLUTION OF THE HEAT TRANSFER EQUATION IN A BISPHERICAL COORDINATE SYSTEM

The energy equation in general orthogonal coordinates is

$$V_\alpha\frac{1}{h_1}\frac{\partial T}{\partial\alpha} + V_\beta\frac{1}{h_2}\frac{\partial T}{\partial\beta} = \frac{\lambda}{\rho C_P}\frac{1}{h_1h_2h_3}\left[\frac{\partial}{\partial\alpha}\left(\frac{h_2h_3}{h_1}\frac{\partial T}{\partial\alpha}\right) + \frac{\partial}{\partial\beta}\left(\frac{h_1h_3}{h_2}\frac{\partial T}{\partial\beta}\right)\right]. \quad (35)$$

The dimensionless energy equation in bispherical ordinates is

$$V_\eta\frac{\partial T^*}{\partial\eta} + V_\theta\frac{\partial T^*}{\partial\theta} = \frac{1}{Re_a\,Pr(h_1/a)}\times\left[\frac{1}{(h_3/a)}\frac{\partial(h_3/a)}{\partial\eta}\frac{\partial T^*}{\partial\eta} + \frac{1}{(h_3/\alpha)}\frac{\partial(h_3/a)}{\partial\psi}\frac{\partial T^*}{\partial\theta}\right] + \frac{1}{Re_a\,Pr(h_1/a)}\left[\frac{\partial^2T^*}{\partial\eta^2} + \frac{\partial^2T^*}{\partial\theta^2}\right] \quad (36)$$

the dimensionless temperature $T^*$ being defined as

$$T^* = \frac{T - T_s}{T_\infty - T_s}. \quad (37)$$

† See conclusions.

Recalling the expressions for $h_1$ and $h_3$ we find

$$\frac{\partial v(h_3/a)}{\partial\eta} = \frac{-1}{F^2}\frac{\partial F}{\partial\eta} = -\frac{1}{F^2}F_\eta(\eta,\theta) \quad (38)$$

$$\frac{\partial(h_3/a)}{\partial\theta} = \frac{1}{F_2}\frac{\partial F}{\partial\theta} = -\frac{1}{F^2}F_\theta(\eta,\theta). \quad (39)$$

It is convenient to express $V_\eta$ and $V_\theta$ in terms of the derivatives of the stream function, the dimensionless energy equation becoming

$$-\frac{\partial\psi}{\partial\theta}\frac{\partial T^*}{\partial\eta} + \frac{\partial\psi}{\partial\eta}\frac{\partial T^*}{\partial\theta} = \frac{1}{Re_a\,Pr}\left[1/F\left(\frac{\partial^2T^*}{\partial\theta^2} + \frac{\partial^2T^*}{\partial\theta^2}\right)\right] - \frac{1}{F^2}\left[\frac{\partial T^*}{\partial\eta}F_\eta(\eta,\theta) + \frac{\partial T^*}{\partial\theta}F_\theta(\eta,\theta)\right]. \quad (40)$$

Using the finite-difference scheme as outlined previously for the Navier–Stokes equations, equation (41) written in a centered-difference (second-order accurate) form becomes

$$-\frac{\langle S(I,J+1)-S(I,J-1)\rangle\langle T^*(I+1,J)-T^*(I-1,J)\rangle}{4DADB} + \frac{\langle S(I+1,J)-S(I-1,J)\rangle\langle T^*(I,J+1)-T^*(I,J-1)\rangle}{4DADB}$$

$$= \frac{1}{Re_a\,Pr\,F(I,J)}\left[\frac{T^*(I+1,J)+T^*(I-1,J)}{DA^2} + \frac{T^*(I,J+1)+T^*(I,J-1)}{DB^2} - T^*(I,J)\right]\times\left(\frac{2}{DA^2} - \frac{2}{DB^2}\right)\Bigg] + \frac{1}{Re_a\,Pr\langle F(I,J)\rangle^2}\times\left[\frac{T^*(I+1,J)-T^*(I-1,J)}{2DA}F_\eta(I,J) + \frac{T^*(I,J+1)-T^*(I,J-1)}{2DB}F_\theta(I,J)\right]. \quad (41)$$

The boundary conditions for this equation are:

(a) on the two spheres $T^* = 0$,

(b) on the axis of symmetry ($\theta = 0$ and $\pi$) $\partial T^*/\partial\theta = 0$,

(c) on the outer edge of the computational domain ($\theta = \theta_{\min}\langle\eta\rangle$), $T^* = 1$.

Equation (41) has been solved using boundary conditions (a)–(c) by an SOR technique with a relaxation factor of 1.2. The temperature at each iteration is calculated as

$$T^*_{n+1}(I,J) = T^*_n(I,J) + WT(T^*_{n+1}(I,J) - T^*_n\langle I,J\rangle). \quad (42)$$

CPU time for solving the energy equation is typically 3 min on a DEC-20 system.

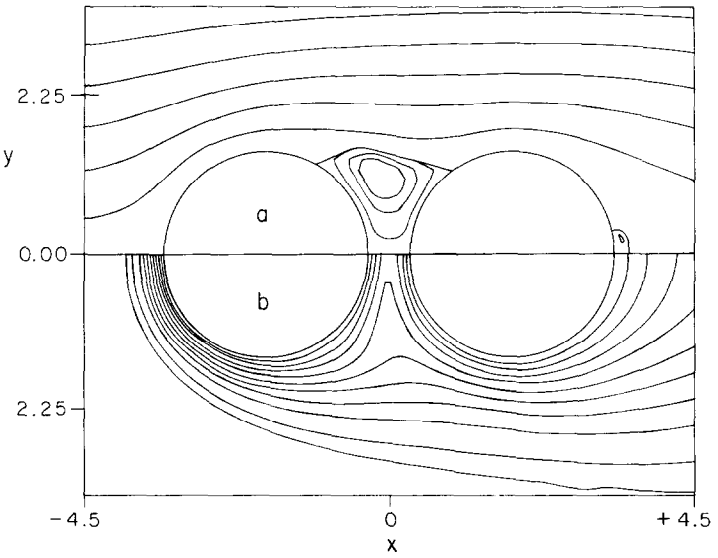


FIG. 2. (a) Streamlines and (b) isotherms for contacting case ($Re = 40$, $Pr = 1$, $2b/d = 1.2$).

## 4. RESULTS

(1) The streamline and isotherm patterns are given in Fig. 2 for a case where the recirculation zone of the upstream sphere contacts the downstream sphere ($Re = 40$, $Pr = 1$, $2b/d = 1.2$), to be referred to subsequently as the contacting case and in Fig. 3 for a case where the recirculation zone of the upstream sphere does not contact the downstream sphere ($Re = 40$, $Pr = 1$, $2b/d = 2.5$), to be referred to as the non-contacting case. In the contacting case, the stagnation type flow on the front hemisphere of the downstream sphere is replaced by a recirculation type zone, which results in a considerable reduction in the drag coefficient and Nusselt number, as will be detailed subsequently. In the non-contacting case, even then the recirculation zone of the upstream sphere does not extend onto the downstream sphere and thus the forward hemisphere of the latter experiences a stagnation type flow, this flow has to accelerate from the stagnation point at the apex of the recirculation zone of the upstream sphere and will be quite slow. As it can be noted from the isotherm patterns for both cases the maximum local Nusselt number (indicated by the maximum density of isotherms) on the downstream sphere is located far away from the front stagnation point. The recirculation zone of the downstream sphere is strongly affected by the presence of the upstream sphere, in both cases. One should keep in mind that in the non-contacting case, though the downstream sphere is not located in the recirculation zone of the upstream sphere, it still is in its wake, experiencing a highly non-uniform upstream velocity profile.

Separation occurs earlier on the upstream sphere and much later on the downstream sphere, for both cases.

The length of the recirculating zone as well as the separation angle are given in Table 1, with the experimental values of Taneda [14] for an isolated single sphere as a reference.

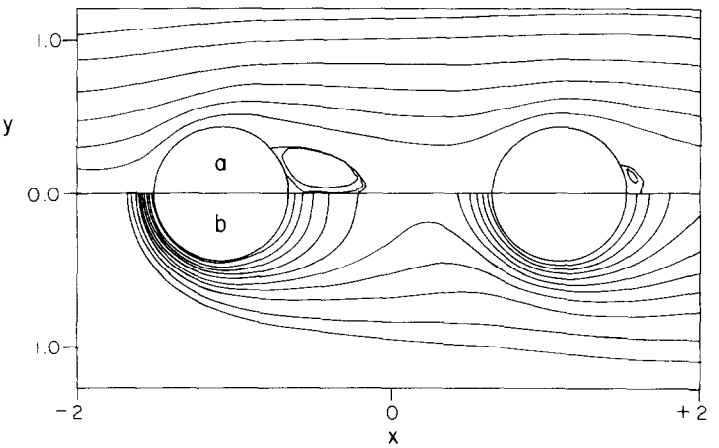


FIG. 3. (a) Streamlines and (b) isotherms for non-contacting case ($Re = 40$, $Pr = 1$, $2b/d = 2.5$).

Table 1. Angles of separation and recirculating zone length

| | $2b/d = 1.2$ | | $2b/d = 2.5$ | |
|---|---|---|---|---|
| | $l_R/(d/2)$ | $\theta_{ps}$ | $l_R/(d/2)$ | $\theta_{ps}$ |
| Upstream sphere | † | 121° | 1.07 | 139° |
| Downstream sphere | 0.12 | 167° | 0.22 | 161° |
| Isolated single sphere | 0.68 | 145° | 0.68 | 145° |

† Recirculating zone in this case extends into downstream sphere.

(2) The pressure coefficient distribution on both spheres compared with that of a single sphere at the same Reynolds number, is given in Fig. 4 for the non-contacting case and in Fig. 5 for the contacting case. It is interesting to note that the pressure distribution on the front stagnation zone of the upstream sphere (the high pressure zone) is not affected by the presence of the downstream sphere. Subsequently, the pressure drops less rapidly, its base pressure being somewhat higher than that corresponding to an isolated single sphere.

The overall effect is a decrease in the pressure drag coefficient of the upstream sphere. The strongest interaction effect is a radical change in the pressure distribution over the surface of the downstream sphere. A low pressure zone is created on the front hemisphere of the downstream sphere, resulting in a considerable

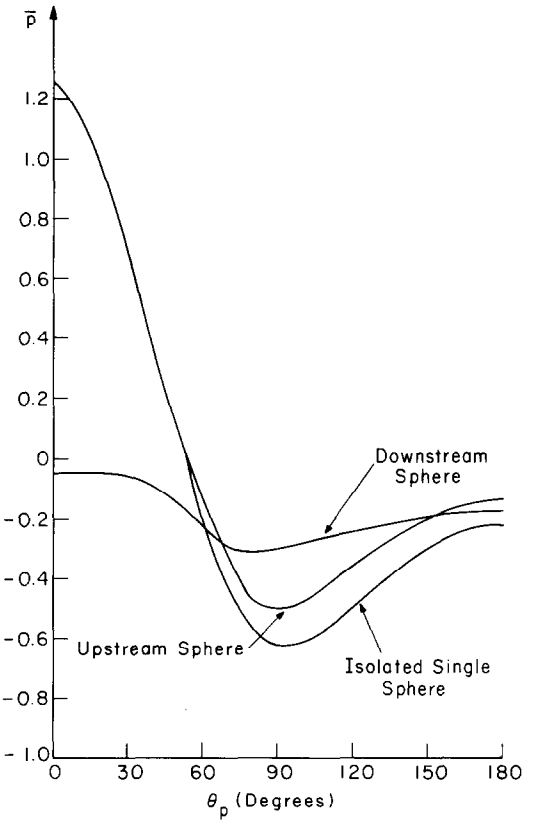


FIG. 5. Pressure vs $\theta_p$ for non-contacting case.

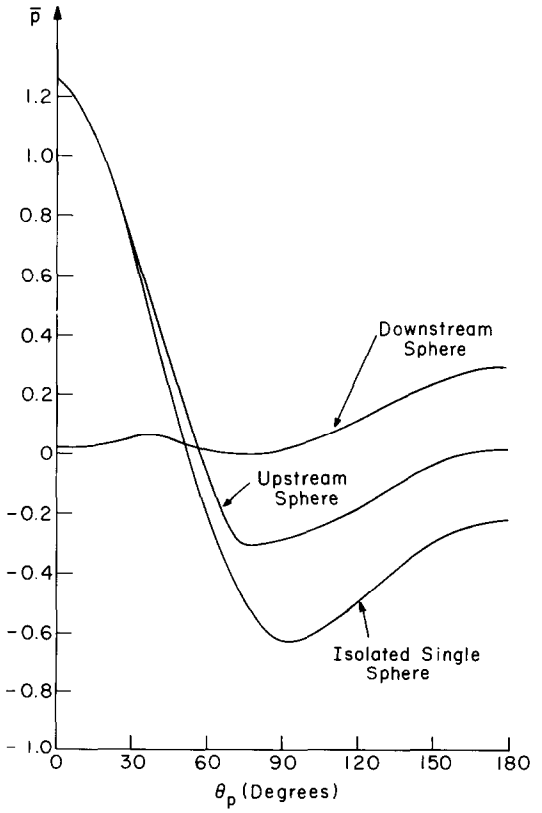


FIG. 4. Pressure vs $\theta_p$ for contacting case.

reduction of the pressure drag. For the contacting case, there is no pressure recovery from the aft stagnation point of the upstream sphere to the front stagnation point of the downstream sphere. The pressure on the aft hemisphere for $2b/d = 1.2$ is higher than on its front hemisphere, resulting in a negative pressure drag, i.e. thrust. (Note that due to friction drag, the total drag coefficient on the sphere is positive.) There is a local maximum of the pressure distribution at $\theta_p = 40°$, probably due to the reattachment of the flow. For the non-contacting case, there is some pressure recovery from the aft stagnation point of the upstream sphere to the front stagnation point of the downstream sphere; the pressure drag on the downstream sphere is considerably reduced, but is still positive.

Friction drag is reduced on both spheres as a result of the reversal of the flow direction as well as the slower flow in the recirculation zones.

Table 2 summarizes the values of the drag coefficients compared to those of a single sphere (the reference case) as well as with the experimental data by Rowe and Henwood [10] measured in the range $Re = 32$–$96$. The agreement with experimental results is quite good, especially when considering the spread of the experimental data. The calculated values tend to overestimate the drag on the upstream sphere and underestimate the drag on the downstream sphere, but are all in the 10% accuracy range.

(3) Local and average Nusselt numbers.

Table 2. Drag coefficients for a pair of spheres in tandem, $Re = 40$

| | $2b/d = 1.2$ | | | | | $2b/d = 2.5$ | | | | |
|---|---|---|---|---|---|---|---|---|---|---|
| | $C_{DP}$ | $C_{DF}$ | $C_{DT}$ | $C_D/C_{D,ref}$† | $(C_D/C_{D,ref})_{exp}$‡ | $C_{DP}$ | $C_{DF}$ | $C_{DT}$ | $C_D/C_{D,ref}$† | $(C_D/C_{D,ref})_{exp}$‡ |
| First sphere | 0.62 | 0.92 | 1.54 | 0.74 | 0.71 | 0.73 | 1.09 | 1.82 | 0.88 | 0.80 |
| Second sphere (downstream) | −0.13 | 0.89 | 0.76 | 0.37 | 0.41 | 0.09 | 1.02 | 1.11 | 0.53 | 0.54 |
| Isolated single sphere (reference) | 0.84 | 1.23 | 2.07 | — | — | 0.84 | 1.23 | 2.07 | — | — |

† Calculated.
‡ Experimental [10].

The local Nusselt number distribution for the contacting case is given in Fig. 6. Observing the Nusselt number on the upstream sphere, we note that there is no difference compared to the case of an isolated single sphere up to a polar angle of 30°, and from here on, the local Nusselt number starts dropping faster than in the case of an isolated single sphere. There is a slight kink in the curve at the outset of separation. On the downstream sphere there is a very significant reduction of the Nusselt number on the front hemisphere (due to the fact that the recirculating zone of the upstream sphere extends onto the downstream sphere). The maximum of the local Nusselt number is at 110°! After this maximum, the Nusselt number drops less rapidly than for the case of an isolated single sphere, because of the highly reduced dimensions of the recirculation zone on the downstream sphere. Overall, the Nusselt number on the upstream sphere is reduced by a factor of 0.85 and on the downstream sphere by a factor of 0.53 (see Table 3).

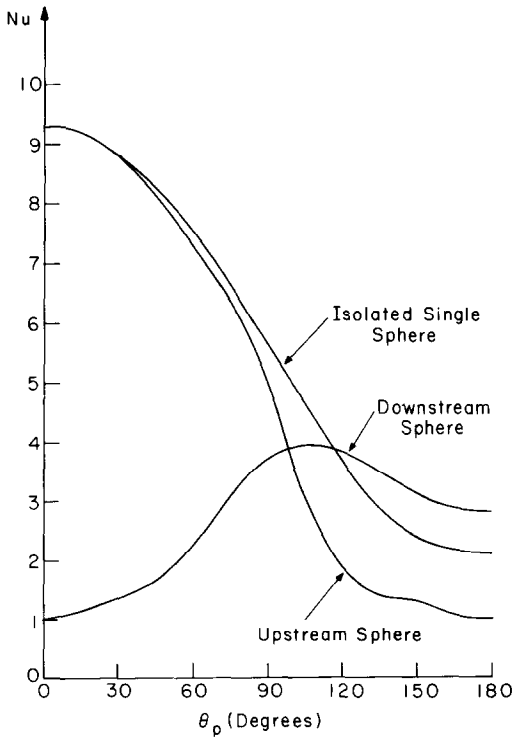


FIG. 6. Local Nusselt number vs $\theta_p$ for contacting case.

For the non-contacting case ($2b/d = 2.5$), the situation is similar (see Fig. 7). There is no difference compared to an isolated single sphere up to a polar angle of 65°; subsequently the Nusselt number drops more rapidly for the interacting case. On the downstream sphere, the peak of the Nusselt number is achieved at a polar angle of 47° (as mentioned previously, the flow in the front stagnation region is very slow as it accelerates from the rear apex of the recirculating zone of the upstream sphere). The values of the average Nusselt number are given in Table 3.

## 5. DISCUSSION AND CONCLUSIONS

The numerical method used is based on equal spacing of the mesh points in the $\eta$–$\theta$ domain. This is convenient for the finite-differencing of the differential equations, but results in non-equal spacing of the mesh points in the physical domain. As a matter of fact, more than 50% of the mesh points are located within the half-circle connecting the two focal points of the bispherical coordinate system ($\pi/2 \leqslant \theta \leqslant \pi$). A very fine resolution is obtained in the recirculatory zone between the two spheres and the resolution decreases at regions more remote from the spheres. However, from the computational (convergence) point of view, a non-uniform spacing of the grid in the $\eta$–$\theta$ domain, such as used by the authors for the problem of interaction between spheres in an assemblage would be preferable [15]. The introduction of such a non-uniform grid, though straightforward in principle, would significantly complicate the finite-differencing of the differen-

Table 3. Average Nusselt numbers for a pair of spheres in tandem, $Re = 40$, $Pr = 1$

| | $2b/d = 1.2$ | | $2b/d = 2.5$ | |
|---|---|---|---|---|
| | $Nu$ | $Nu/Nu_{ref}$ | $Nu$ | $Nu/Nu_{ref}$ |
| First (upstream) sphere | 4.81 | 0.85 | 5.35 | 0.95 |
| Second (downstream) sphere | 2.99 | 0.53 | 3.54 | 0.63 |
| Unconfined sphere | 5.63 | — | 5.63 | — |

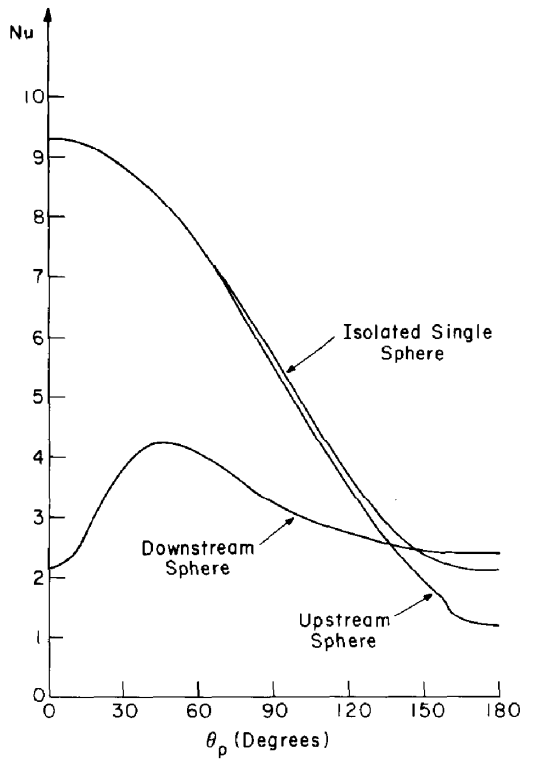


FIG. 7. Local Nusselt number vs $\theta_p$ for non-contacting case.

tial equations, which involved significant effort even for the uniform spacing. The fact that introducing the non-uniform grid has not been pursued is the principal reason for not considering a variety of spacings and Reynolds number values. In fact, as indicated by Rowe and Henwood [10] and according to the results of Tsuji *et al.* [11], interaction effects are not very sensitive to the Reynolds number. The main reason for this might well be the fact that tandem interactions are more pressure drag effects than friction drag effects.

The cases solved give an important insight into the physical nature of the interaction between two spheres in tandem. The conclusions can be summarized as follows:

(1) The pressure drops less rapidly (compared to an isolated single sphere) on the upstream sphere, resulting in a lower pressure drag. On the front hemisphere of the downstream sphere, a low pressure area is created. The drag coefficient is reduced for both spheres in tandem as compared with a single sphere, the reduction being more significant for the downstream sphere. The drag coefficient results are in good agreement with experimental results.

(2) The Nusselt number is reduced slightly on the upstream sphere and significantly on the downstream sphere. The shape of the local Nusselt number distribution is totally altered on the downstream sphere, the maximum no more being located at the front stagnation point.

(3) The pressure distribution as well as the local Nusselt number close to the front stagnation point of the upstream sphere are unaffected by the downstream sphere.

(4) Our results are in good quantitative agreement with the experiments of Rowe and Henwood [10] performed for the applicable range of the present work, as well as in qualitative agreement with the theoretical and experimental works of Stimson and Jeffrey [12], Aminzadeh *et al.* [13] and Tsuji *et al.* [11], performed for pairs of spheres under much different conditions of Reynolds numbers.

(5) The method used in this paper is ideally suited for a pair of spheres, but the coordinate system has not been generalized for more than two spheres.

## REFERENCES

1. E. M. Twardus and T. A. Brzustowski, The interaction between two burning fuel droplets, 5th Int. Symp. on Combustion Processes, Krakow, Poland, September (1972).
2. A. Umemura, S. Ogawa and N. Oshima, Analysis of the interaction between two burning droplets, *Combust. Flame* **41**, 35–44 (1981).
3. A. Umemura, S. Ogawa and N. Oshima, Analysis of the interaction between two burning fuel droplets with different sizes, *Combust. Flame* **43**, 111–191 (1981).
4. M. Labowsky, Calculation of the burning rates of interacting fuel droplets, *Combust. Sci. Technol.* **22**, 217–220 (1980).
5. F. R. Rex, A. E. Fahs and S. S. Penner, Interference effects during burning in air for stationary n-heptane, ethyl alcohol and methyl alcohol droplets, *Jet Propulsion* **26**, 179–187 (1956).
6. J. J. Sangiovanni and D. S. Kesten, An experimental study of the ignition and combustion characteristics of fuel droplets, United Technologies Research Center Report R76-952, p. 180 (1976).
7. S. Prakash and W. A. Sirignano, Liquid fuel droplet heating with internal circulation, *Int. J. Heat Mass Transfer* **21**, 885 (1978).
8. S. Prakash and W. A. Sirignano, Theory of convective droplet vaporization with unsteady heat transfer in the circulating liquid phase, *Int. J. Heat Mass Transfer* **23**, 253 (1980).
9. P. Lara-Urbaneja and W. A. Sirignano, Theory of transient multicomponent droplet vaporization in a convective field, *Proc. 19th Int. Symp. on Combustion*, Combustion Institute (1981).
10. P. N. Rowe and G. A. Henwood, Drag forces in a hydraulic model of a fluidized bed—Part I, *Trans. Instn Chem. Engrs* **39**, 43–54 (1961).
11. Y. Tsuji, Y. Morikawa and K. Terashima, Fluid-dynamic interaction between two spheres, *Int. J. Multiphase Flow* **8**, 71–82 (1982).
12. M. Stimson and G. B. Jeffrey, The motion of two spheres in a viscous fluid, *Proc. R. Soc.* **A11**, 110–116 (1926).
13. K. Aminzadeh, T. R. Al Taha, D. R. M. Cornish, M. S. Kolansky and R. Pfeffer, Mass transport around two spheres at low Reynolds numbers, *Int. J. Heat Mass Transfer* **17**, 1425–1436 (1974).
14. S. Taneda, Experimental investigation of the wake behind a sphere at low Reynolds numbers, *Rep. Res. Int. Appl. Mech. Kyushu Univer.* **4**, 99 (1956).
15. R. Tal (Thau), D. N. Lee and W. A. Sirignano, Hydrodynamics and heat transfer in sphere assemblages—multisphere cylindrical cell models, AIAA paper 82-0302, AIAA 20th Aerospace Sciences Meeting, Orlando, Florida (1982).

## TRANSFERT DE CHALEUR ET DE QUANTITE DE MOUVEMENT AUTOUR D'UNE PAIRE DE SPHERES DANS UN ECOULEMENT VISQUEUX

**Résumé**—Les équations de Navier–Stokes et de l'énergie sont résolues numériquement pour une paire de sphères en tandem à $Re = 40$, pour deux espacements différents, en utilisant des coordonnées bisphériques. Les solutions sont comparées favorablement avec des résultats expérimentaux. Le coefficient de trainée et le nombre de Nusselt moyen sur chacune des sphères est toujours moindre que pour une sphère unique, l'effet étant plus fort sur la sphère en aval.

## WÄRME- UND IMPULSÜBERTRAGUNG AN EINEM KUGELPAAR BEI ZÄHER STRÖMUNG

**Zusammenfassung**—Die Navier–Stokes- und die Energiegleichungen wurden für ein Kugelpaar in Tandem-Anordnung für zwei verschiedene Abstände bei $Re = 40$ unter Verwendung von Bipolar-Koordinanten numerisch gelöst. Die Lösungen stimmen gut mit experimentellen Ergebnissen überein. Der Widerstandsbeiwert und die mittlere Nusselt-Zahl sind immer kleiner als bei einer einzelnen, isolierten Kugel; besonders ausgeprägt zeigt sich dies an der stromab liegenden Kugel.

## ПЕРЕНОС ТЕПЛА И ИМПУЛЬСА ОКОЛО ДВУХ СФЕР В ПОТОКЕ ВЯЗКОЙ ЖИДКОСТИ

**Аннотация**—В бисферической системе координат проведено численное решение уравнений Навье–Стокса и энергии для двух последовательно расположенных сфер при $Re = 40$ для двух различных расстояний между ними. Результаты решения хорошо согласуются с экспериментальными данными. Показано, что значения коэффициента сопротивления и среднего числа Нуссельта для каждой сферы в паре меньше значений для единичной изолированной сферы, причем этот эффект проявляется наиболее заметно для сферы, расположенной вниз по потоку.